

This is the accepted manuscript made available via CHORUS. The article has been published as:

## Reflection thermal diffuse x-ray scattering for quantitative determination of phonon dispersion relations

A. B. Mei, O. Hellman, C. M. Schlepütz, A. Rockett, T.-C. Chiang, L. Hultman, I. Petrov, and J. E. Greene

Phys. Rev. B **92**, 174301 — Published 3 November 2015

DOI: [10.1103/PhysRevB.92.174301](https://doi.org/10.1103/PhysRevB.92.174301)

# Reflection thermal diffuse x-ray scattering for quantitative determination of phonon dispersion relations

A. B. Mei,<sup>1</sup> O. Hellman,<sup>2</sup> C. M. Schlepütz,<sup>3,4</sup> A. Rockett,<sup>1</sup>  
T.-C. Chiang,<sup>5</sup> L. Hultman,<sup>6</sup> I. Petrov,<sup>1,6</sup> and J. E. Greene<sup>1,6</sup>

<sup>1</sup> Department of Materials Science and the Materials Research Laboratory  
University of Illinois, 104 South Goodwin, Urbana, IL 61801

<sup>2</sup> Department of Applied Physics and Materials Science,  
California Institute of Technology, Pasadena, California 91125, USA

<sup>3</sup> X-ray Science Division, Advanced Photon Source,  
Argonne National Laboratory, 9700 S. Cass Avenue, Argonne, Illinois 60439, USA

<sup>4</sup> Swiss Light Source, Paul Scherrer Institut, 5232 Villigen PSI, Switzerland

<sup>5</sup> Department of Physics and the Materials Research Laboratory  
University of Illinois, 1110 West Green Street, Urbana, IL 61801

<sup>6</sup> Thin Film Physics Division, Department of Physics (IFM)  
Linköping University, SE-58183 Linköping, Sweden

## Abstract

Synchrotron reflection x-ray thermal diffuse scattering (TDS) measurements, rather than previously reported transmission TDS, are carried out at room temperature and analyzed using a formalism based upon second-order interatomic force constants and long-range Coulomb interactions to obtain quantitative determinations of MgO phonon dispersion relations  $\hbar\omega_j(\mathbf{q})$ , phonon densities of states  $g(\hbar\omega)$ , and isochoric temperature-dependent vibrational heat capacities  $c_v(T)$ . We use MgO as a model system for investigating reflection TDS due to its harmonic behavior as well as its mechanical and dynamic stability. Resulting phonon dispersion relations and densities of states are found to be in good agreement with independent reports from inelastic neutron and x-ray scattering experiments. Temperature-dependent isochoric heat capacities  $c_v(T)$ , computed within the harmonic approximation from  $\hbar\omega_j(\mathbf{q})$  values, increase with temperature from  $0.4 \times 10^{-4}$  eV/(atom K) at 100 K to  $1.4 \times 10^{-4}$  eV/(atom K) at 200 K and  $1.9 \times 10^{-4}$  eV/(atom K) at 300 K, in excellent agreement with isobaric heat capacity values  $c_p(T)$  between 4 and 300 K. We anticipate that the experimental approach developed here will be valuable for determining vibrational properties of heteroepitaxial thin films since the use of grazing-incidence ( $\theta \lesssim \theta_c$ , where  $\theta_c$  is the density-dependent critical-angle) allows selective tuning of x-ray penetration depths to  $\lesssim 10$  nm.

## I. Introduction

Phonons, elementary quanta of lattice vibrations, are well known to control high-temperature transport and structural properties of crystalline solids [1–7]. As a result, the ability to spectrally resolve phonon energies has proven central to the understanding of fundamental materials properties. Techniques by which phonon energies  $\hbar\omega_j$ , in which  $\hbar$  is the reduced Planck constant and  $\omega_j$  the angular frequency of phonon branch  $j$ , may be obtained include Raman [8] and tunneling spectroscopy [9]. Often, however, crystal properties are strongly influenced by phonons with specific momenta; archetype examples are systems exhibiting charge density waves [2] and Kohn anomalies [1]. In such cases, a deeper understanding of crystalline properties requires determination of dispersion relations  $\hbar\omega_j(\mathbf{q})$  in which both phonon momenta  $\mathbf{q}$  and energies  $\hbar\omega_j$  are resolved. Historically,  $\hbar\omega_j(\mathbf{q})$  curves have been determined by inelastic x-ray and neutron scattering. These techniques, nevertheless, require complex experimental equipment, long acquisition times, and, in the case of neutron scattering, large single crystals. The latter restriction eliminates many interesting thin-film systems such as highly-strained heterostructures and metastable materials.

Recently, transmission thermal diffuse x-ray scattering (TDS) has become an efficient experimental alternative for determining phonon dispersion relations. TDS experiments involve the detection of x-ray photons which are quasi-elastically scattered from thermally-excited atoms vibrating about their equilibrium position. Displaced atoms break the symmetry of the ideal crystal, resulting in scattering away from Bragg peaks. Atomic displacements accompanying zone-boundary X-point phonons in face-centered cubic materials, for example, yield an irreducible superstructure which is double the size of the ideal unit cell. As a result, TDS intensities due to X-point phonons appear halfway between Bragg reflections at reciprocal space positions described by mixed-integer Miller indices, e.g.  $[0\ 0\ 1]$  and  $[1\ 1\ 0]$ . Pioneering work by Chiang, Holt, and coworkers demonstrated the capabilities of TDS measurements by determining  $\hbar\omega_j(\mathbf{q})$  phonon dispersion curves for Si [10], Ga-stabilized Pu [11],  $\text{TiSe}_2$  [12], and Cu [13] crystals. However, TDS experiments are presently carried out in transmission geometry and, as a result, samples are limited to bulk crystals.

Thin films represent a technologically important class of materials for which the number of sample types is increasingly growing. In particular, novel metastable phases, inaccessible by bulk synthesis techniques, can be produced using kinetically-limited growth processes [14–21]

and epitaxial constraints [22–27]. Despite the importance of thin films, there are only a restricted number of methods [28,29] for determining phonon dispersion relations for this class of materials.

Here, we introduce a TDS technique for determining phonon dispersions  $\hbar\omega_j(\mathbf{q})$  and densities of states  $g(\hbar\omega)$  based on a reflection scattering configuration. We demonstrate the method using MgO as a model materials system. It is anticipated that the results presented here will be beneficial for selectively determining vibrational properties of heteroepitaxial thin films, since x-ray penetration depths may be tuned through the use of grazing incidence geometries. From thermal-diffuse x-ray pole figures, we determine  $\hbar\omega_j(\mathbf{q})$  and  $g(\hbar\omega_j)$  and compute, via the harmonic approximation, temperature-dependent isochoric MgO heat capacities  $c_v(T)$ . MgO is chosen for this study due to its nearly harmonic behavior as well as mechanical and dynamic stability [30]. Pole figures are measured about an 011 oriented sample normal, since this primary cubic direction exhibits lower symmetry, two-fold, and thus allows the sampling of a higher number of unique reciprocal space points than the four-fold symmetric 001 and three-fold symmetric 111 orientations.

## II. Experimental procedures

Thermal-diffuse synchrotron x-ray pole figure measurements are collected at beamline 33-BM of the Advanced Photon Source, Argonne National Laboratory. Experiments are performed with the storage ring operating in top-up mode with an electron energy of 7 GeV and a stored current of 100 mA. Using a double-crystal Si(111) monochromator, the wavelength of the x-ray probe beam is set to 0.05904 nm (21 keV). Polished MgO(011) sample wafers, 5x5 mm<sup>2</sup>, are obtained from the MTI Corporation. To minimize air scattering during measurements, samples are enclosed in a Be-dome-covered stage and evacuated to 1x10<sup>-6</sup> Torr (1.3 x10<sup>-4</sup> Pa). Scattering from the Be-dome is eliminated by placing collimating slits close to the sample holder. The x-ray probe beam is focused onto the detector plane, yielding 1x10<sup>12</sup> photons/s incident on an 800x400 μm<sup>2</sup> area of the sample surface. Beam divergence, which is almost exclusively in the horizontal plane of the synchrotron, is ~ 4 mrad and has a negligible effect on resolution when compared the typical size of thermal diffuse features, spanning several degrees. All scattering experiments are performed in the vertical plane of the synchrotron to avoid polarization effects. Scattering intensities are recorded at each pixel of a Pilatus 100K area

detector to produce four hundred individual pole-figures over azimuthal angles  $\chi = 0-80^\circ$  and rotational angles  $\varphi = 0-360^\circ$ , covering diffraction vectors ranging from  $q = 42.60$  to  $70.32 \text{ nm}^{-1}$ . The resulting data set encompasses over a million individually-sampled reciprocal space points.

### III. Theoretical procedures

#### A. MgO phonon dispersion relations

In order to obtain MgO phonon dispersion relations  $\hbar\omega_j(\mathbf{q})$ , phonon densities of states  $g(\hbar\omega)$ , and temperature-dependent vibrational heat capacities  $c_v(T)$ , thermal diffuse intensities are computed based on an eleven-parameter Born-von-Karman model which incorporates short-range second-nearest-neighbor interatomic interactions and long-range Coulomb interactions. Model parameters, including MgO high-frequency dielectric constants, Born effective charges, and interatomic force constants, are then iteratively adjusted using a hybrid simulated annealing and robust nonlinear least-squares minimization routine until the best match between theoretical and experimental diffracted intensities is obtained. Simulated annealing is a stochastic metaheuristic optimization algorithm that searches for the global minimum, while avoiding local minima traps. Least-squares routines utilize Hessians to converge efficiently once the neighborhood of a global minimum is found.

MgO phonon dispersion relations  $\hbar\omega_j(\mathbf{q})$  and phonon eigenvectors  $\boldsymbol{\varepsilon}_j(\mathbf{q})$ , corresponding to vibrational energies and atomic displacements associated with specific phonon wavevectors, are obtained by diagonalizing dynamical matrices  $\mathbf{D}(\mathbf{q})$ :

$$\mathbf{D}(\mathbf{q})\boldsymbol{\varepsilon}_j(\mathbf{q}) = \omega_j^2(\mathbf{q})\boldsymbol{\varepsilon}_j(\mathbf{q}). \quad (1)$$

For crystals with  $n$  atoms in the primitive unit cell,  $\mathbf{D}(\mathbf{q})$ ,  $\boldsymbol{\varepsilon}_j(\mathbf{q})$ , and  $\omega_j^2(\mathbf{q})$  are matrices with dimensions  $3n \times 3n$ . In ionic crystals, such as MgO, dynamical matrices consist of two contributions:

$$\mathbf{D}(\mathbf{q}) = \mathbf{D}_I(\mathbf{q}) + \mathbf{D}_C(\mathbf{q}). \quad (2)$$

$\mathbf{D}_I(\mathbf{q})$  describes short-range interatomic forces and  $\mathbf{D}_C(\mathbf{q})$  represents long-range Coulomb interactions. The elements of short-range dynamical matrices are obtained by Fourier

transforming interatomic force constants  $\Phi$ :

$$\mathbf{D}_I(\mathbf{q}) \equiv \mathbf{D}_{s,s'}^{\alpha,\beta}(\mathbf{q}) = \frac{1}{\sqrt{\mu_s \mu_{s'}}} \sum_{m'} \Phi_{s,m,s',m'}^{\alpha,\beta} \exp[i\mathbf{q} \cdot \mathbf{R}_{m,m'}]. \quad (3)$$

Here,  $s$  and  $s'$  are indices of the two basis atoms in the primitive fcc unit cell,  $m$  and  $m'$  correspond to two different primitive unit cells, and  $\alpha$  and  $\beta$  are two of the three Cartesian directions.  $\mu_s$  is the mass of atom  $s$ , and  $\mathbf{R}_{m,m'}$  is the distance between unit cells  $m$  and  $m'$ . To reproduce MgO atomic vibrations with the smallest number of parameters, we consider only second-nearest-neighbor interactions and employ full crystal symmetry operations. This reduces the number of interatomic force constants from over eight hundred to only eight independent values.

In the continuum limit (i.e.  $q \approx 0$ ), Cochran and Cowley [31] showed that the long-range dynamical matrix, which describes Coulomb interactions and gives rise to Lyddane-Sachs-Teller [32] splitting of transverse and longitudinal optical phonon modes (TO and LO), reduces to

$$\tilde{\mathbf{D}}_C(\mathbf{q}) = \frac{e^2}{\epsilon_0 V} \frac{[\mathbf{q} \mathbf{Z}^*(s)]_\alpha [\mathbf{q} \mathbf{Z}^*(s')]_\beta}{\mathbf{q} \cdot \boldsymbol{\epsilon}_\infty \cdot \mathbf{q}}. \quad (4)$$

$\mathbf{Z}^*(s)$  is the Born effective charge tensor of atom  $s$ ,  $\boldsymbol{\epsilon}_\infty$  is the high-frequency dielectric tensor,  $\epsilon_0$  is the permittivity of free space,  $e$  the electron charge, and  $V$  the unit-cell volume. For cubic materials,  $\mathbf{Z}^*$  and  $\boldsymbol{\epsilon}_\infty$  are scaled identity matrices. In order to simulate the effect of Coulomb interactions throughout the Brillouin zone, long-range dynamical matrices are constructed using a Fourier interpolation scheme based on Cochran and Cowley's results [33]:

$$\mathbf{D}_C(\mathbf{q}) = \tilde{\mathbf{D}}_C(\mathbf{q}) \left\{ \cos\left(\frac{|\mathbf{q}|}{q_{\max}}\right)^r \right\}. \quad (5)$$

The term in curly brackets is an interpolating function,  $q_{\max}$  is the magnitude of the largest wavevector in the first Brillouin zone, and  $r$  is an empirical cutoff parameter describing the

spread of the Coulomb interaction away from the zone center.

Together, Eqs. 1-4 fully describe the wavevector and energy dependence of all MgO lattice vibrations via eleven material parameters: the Born effective charge, the high-frequency dielectric constant, a Coulomb interaction cutoff parameter, and eight second-nearest-neighbor interatomic force constants.

### B. Thermal diffuse scattering intensities

Thermal diffuse scattering intensities are computed using the relationship [10,34]

$$I(\mathbf{q}) = A \left[ \frac{\hbar N I_e}{2} \sum_j \frac{1}{\hbar \omega_j(\mathbf{q})} \coth \left( \frac{\hbar \omega_j(\mathbf{q})}{2 k_B T} \right) |F_j(\mathbf{q})|^2 \right] + B, \quad (6)$$

in which  $N$  is the number of unit cells in the crystal,  $I_e$  the scattering intensity from a single electron [35], and  $k_B$  is Boltzmann's constant. The summation is carried out over phonon branch indices  $j$ . The term in square brackets corresponds to first-order thermal-diffuse scattering intensities; higher-order terms, together with Compton scattering effects [35,36], are included via the empirical parameter  $B$ . The scaling parameter  $A$  controls the relative strength of first-order diffuse scattering intensities. In the limit of small phonon energies  $\hbar \omega_j(\mathbf{q})$ , the hyperbolic cotangent term describing the increasing phonon thermal population increases as  $2k_B T / \hbar \omega_j(\mathbf{q})$  causing the intensity to increase at wavevectors close to  $\Gamma$  Brillouin-zone centers, i.e. Bragg reflections, where low-energy phonons exist in large populations:  $I(\mathbf{q}) \propto 1/[\hbar \omega_j(\mathbf{q})^2 + \beta]$ .  $\beta$  accounts for the fact that the thermal population around  $\Gamma$  is always finite.

The structure factor for the  $j^{\text{th}}$  phonon branch is

$$F_j(\mathbf{q}) = \sum_s \frac{f_s}{\sqrt{\mu_s}} \exp[-M_s(\mathbf{q})] [\mathbf{q} \cdot \boldsymbol{\epsilon}_{j,s}(\mathbf{q})] \exp(-i\mathbf{q} \cdot \boldsymbol{\tau}_s), \quad (7)$$

in which  $f_s$ ,  $\boldsymbol{\tau}_s$ , and  $M_s(\mathbf{q})$  are the atomic scattering factor, atomic coordinates, and Debye-Waller factor of atom  $s$  [35].  $\boldsymbol{\epsilon}_{j,s}(\mathbf{q})$  is the component of the eigenvector corresponding to atom  $s$  and phonon  $j$ .

Thus, MgO thermal-diffuse pole figure intensities depend on an eleven-parameter model, Eqs. 1-5, and two empirical parameters, A and B. By comparing computed thermal-diffuse pole figure intensities to measured values and refining the parameters until the best fit between measured and simulated values is obtained, MgO vibrational properties, including phonon dispersion relations and temperature-dependent isochoric heat capacities, are determined. All subsequent discussion and results are based on the refined material parameters.

### III. Results and discussion

Typical synchrotron x-ray diffraction pole-figures acquired from MgO(011) over the range  $\varphi = 180\text{-}360^\circ$  with diffracting-vector magnitudes  $q = 57.82, 62.61, 64.42, \text{ and } 68.58 \text{ nm}^{-1}$  are presented in Figures 1(a)-(d) as stereographic projections with logarithmically-scaled diffracted intensities corrected for defocus [37–39]. The experimental geometry is defined in Figure 1(e). Simulated thermal-diffuse intensities based on refined model parameters, which include descriptions of interatomic forces and Coulomb interactions, are plotted, for comparison, over rotational angles  $\varphi = 0\text{-}180^\circ$  in Figures 1(a)-(d). Pole figures from 011-oriented cubic crystals are two-fold symmetric about the vertical  $\varphi$  axis. Reciprocal space regions probed in Figures 1(a)-(d) are sufficiently distant from Brillouin-zone centers to avoid Bragg reflections and provide diffracted intensities which arise predominately from atomic vibrations. MgO(011) pole figures are acquired with  $q = 57.82 \text{ nm}^{-1}$  and shown in Figure 1(a) to exhibit two strong diamond-shaped features ( $\chi = 45^\circ$ ;  $\varphi = 90, 270^\circ$ ) and two diffuse triangular features ( $\chi = 35^\circ$ ;  $\varphi = 0, 180^\circ$ ) which arise from thermal acoustic excitations around 002 and 111 Brillouin zone centers [40]. For  $q = 62.61 \text{ nm}^{-1}$ , intensities weaken slightly near 002 and become more diffuse around 111; in addition, ten features appear near 240 zone centers. With increasing  $q$  from 64.42 to  $68.58 \text{ nm}^{-1}$ , Figures 1(c) and (d), thermal diffuse intensities around 002 zone centers continue to decrease. In Figure 1(c), ten small features appear near 313 zone centers; ten additional features appear near 242 zone centers in Figure 1(d). Extracted profiles from measured and simulated thermal diffuse intensities acquired with  $q = 68.58 \text{ nm}^{-1}$ , Figure 1(d), over the range  $\varphi = 0\text{-}360^\circ$  for  $\chi = 20, 50, \text{ and } 70^\circ$  are shown on a logarithmic scale in Figure 2 to be in excellent agreement.

Figures 3(a)-(f) show simulated contributions to thermal-diffuse pole-figure intensities at  $q = 68.58 \text{ nm}^{-1}$  from each of the six MgO(011) phonon branches. The figures are obtained using



Eq. 6 to simulate each mode separately. TDS intensities arising from the lowest-energy acoustic phonon branch are shown in Figure 2(a) and the highest-energy optical phonon branch in Figure 3(f). The sum of the pole-figure intensities from all six phonon branches yield the total thermal-diffuse pole figure intensity presented in Figure 1(d). Since phonons branches are sorted by their eigenvalues, discontinuities in pattern intensities arise from sharp changes in phonon eigenvectors at points in reciprocal space where phonon branches cross. Mathematically, this results from the dot product in Eq. 7; physically, this indicates that lattice vibrations only contribute to scattering if atoms are displaced with a non-zero component parallel to the scattering vector. Diffracted intensities are largest for the three lowest energy phonon modes, Figures 3(a)-(c).

MgO phonon dispersion curves, obtained by simulating thermal-diffuse pole-figure intensities and refining model parameters to match measured results, are plotted along high-symmetry reciprocal-space directions in Figure 4(a). Results from inelastic neutron scattering from MgO crystals [41], shown for comparison, are in good agreement. MgO acoustic phonon energies increase linearly near the  $\Gamma$ -point Brillouin-zone center 000 and saturate toward the X and L zone boundaries 001 and  $\frac{1}{2}\frac{1}{2}\frac{1}{2}$ . The increase near the zone center is greater for longitudinal acoustic phonons, indicating higher propagation group velocities than for transverse phonons. Transverse and longitudinal optical phonon energies, 50 and 90 meV, are distinct at the  $\Gamma$ -point due to long-range Coulomb interactions. While TO modes exhibit weak dispersion, i.e. their energies vary slowly throughout the Brillouin zone, the energies of LO modes decrease rapidly toward X and L zone boundaries. Along the  $X\Gamma$   $[0\zeta\zeta]$  reciprocal-space path, where phonon polarization vectors point along  $[100]$  or  $[0\bar{1}1]$ , both pairs of transverse acoustic and transverse optical phonon branches exhibit unique energies. Along  $\Gamma X$   $[00\zeta]$  and  $\Gamma L$   $[\zeta\zeta\zeta]$  paths, the polarization vectors point along symmetrically equivalent directions; as a result, the energies of the acoustic transverse modes, as well as the optical transverse modes, are degenerate.

The MgO phonon densities of states  $g(\hbar\omega)$ , representing the number of vibrational states per eV-atom, are computed using the relationship

$$g(\hbar\omega) = \frac{1}{N} \sum_j \delta(\hbar\omega_j - \hbar\omega), \quad (8)$$

in which the  $\delta$  is the Dirac delta function. Resulting  $g(\hbar\omega)$  values are presented in Figure 5 together with reported results from density functional theory calculations [33] and inelastic x-ray [42] and neutron [41] scattering measurements. The curves are in good agreement.  $g(\hbar\omega)$  exhibits three primary features centered near  $\hbar\omega = 33, 52$ , and  $70$  meV. These arise from van-Hove singularities in  $\hbar\omega_j(\mathbf{q})$  curves, i.e. points in reciprocal space where phonons have small group velocities and branch energies are approximately constant as a function of wavevector.

Figure 6 shows isochoric MgO heat capacities  $c_v(T)$  over the temperature range 10-400 K. Values are calculated within the harmonic approximation through the integral transform [1,2]

$$c_v(T) = \frac{k_B}{4} \int_0^\infty \left( \frac{\hbar\omega}{2k_B T} \right)^2 \text{csch}^2 \left( \frac{\hbar\omega}{2k_B T} \right) g(\hbar\omega) d\hbar\omega \quad (9)$$

using refined MgO model parameters obtained by fitting room-temperature thermal-diffuse pole-figure intensities. The values obtained are in excellent agreement with reported temperature-dependent isobaric heat capacities  $c_p(T)$  plotted as squares [43] and circles [44–46] in Figure 6. At low temperatures ( $T < 50$  K), for which only long-range acoustic phonons exhibiting linear dispersions are thermally excited, MgO heat capacities increase following a cubic power-law behavior:  $c_v \propto T^3$ . At higher temperatures,  $c_v(T)$  approaches the classical equipartition value,  $c_v = 3k_B = 2.58 \times 10^{-4}$  eV/((atom K)). For  $T = 400$  K, the MgO heat capacity is 85% of the equipartition value; for  $T = 1700$  K, 99%. MgO melts at 3125 K. The fact that MgO heat capacities evaluated at constant volume and measured at constant pressures agree indicates that anharmonic effects, including those resulting from thermal expansion, are negligible at  $T < 400$  K.

As a final point, we consider extending thermal-diffuse x-ray scattering to the analysis of thin films. Since thermal diffuse scattering measurements are not constrained to specific scattering conditions, such as those fulfilling Bragg criteria, sensitivity to surface layers can be achieved by performing asymmetric grazing incidence measurements in which the x-ray beam is fixed at subcritical incidence angles with respect to the sample and diffuse scattering intensities are mapped in reciprocal space by moving only the detector. The x-ray/sample interaction volume is defined by  $\alpha_i$ , the angle between the incident x-ray beam and the surface plane. For  $\alpha_i < \theta_c$ , the critical x-ray angle, total external reflection occurs resulting in evanescent waves which

penetrate only very shallow subsurface regions.  $\theta_c$  depends on the electron density of the exposed layer and the x-ray energy. For 21 keV x-rays ( $\lambda = 0.05904$  nm) impinging on MgO,  $\theta_c = 0.10^\circ$ , yielding a penetration depth of  $\lesssim 10$  nm at  $\theta = 0.09^\circ$ .

Even with a fixed  $\alpha_i$  angle, it is possible to investigate vast regions of reciprocal space by moving the detector. This is illustrated by the following pair of equations which define the relationship between the incident  $\alpha_i$  and outgoing  $\alpha_f$  angles with respect to the surface plane, i.e. the real-space experimental arrangement, and the in-plane  $q_x$  and out-of-plane  $q_z$  reciprocal-space wavevector components [47,48]:  $q_x = [\cos(\alpha_f) - \cos(\alpha_i)]/\lambda$  and  $q_z = [\sin(\alpha_f) + \sin(\alpha_i)]/\lambda$ . Equivalently, in terms of a Bragg-Brentano configuration,  $\omega = \alpha_i$  and  $2\theta = (\alpha_i + \alpha_f)$ ,  $q_x = 2\sin(\theta)\sin(\theta - \omega)/\lambda$  and  $q_z = 2\sin(\theta)\cos(\theta - \omega)/\lambda$ . Thus, comprehensive data sets which sample thermal diffuse scattering intensities over wide regions of reciprocal space with fixed x-ray/sample interaction volume and selective surface sensitivity may be obtained and analyzed using the methods described above to quantitatively determine phonon dispersion relations for thin films with thicknesses as small as  $\sim 10$  nm.

#### 4. Conclusions

We have demonstrated a new method for determining phonon dispersion relations  $\hbar\omega_j(\mathbf{q})$ , phonon densities of states  $g(\hbar\omega)$ , and temperature-dependent vibrational heat capacities  $c_v(T)$  of solids based upon synchrotron thermal-diffuse x-ray scattering pole-figure measurements carried out in the reflection, rather than the previously investigated transmission, geometry. We anticipate that the experimental techniques presented here will be valuable for determining vibrational properties of heteroepitaxial thin films since x-ray penetration depths can be selectively tuned through the use of grazing incidence. In order to illustrate the method, MgO was used as model materials system due to its harmonic behavior and high mechanical and dynamic stability. Resulting MgO phonon dispersion relations and densities of states are found to be in good agreement with independent reports from inelastic neutron and x-ray scattering experiments carried out on single crystals. Temperature-dependent heat capacities obtained within the harmonic approximation at constant volume agree with values measured at constant pressure between 4 and 300 K.

## **5. Acknowledgements**

The authors thank Dr. Mauro Sardela for valuable discussions. The financial support of the Swedish Research Council (VR), the Swedish Government Strategic Research Area Grant in Materials Science (SFO Mat-LiU) on Advanced Functional Materials, and the US Department of Energy, Office of Science, Office of Basic Energy Sciences (TCC under Grant No. DE-FG02-07ER46383) is greatly appreciated. This research used resources of the Advanced Photon Source, a U.S. Department of Energy (DOE) Office of Science User Facility operated for the DOE Office of Science by Argonne National Laboratory under Contract No. DE-AC02-06CH11357.

## 6. References

- [1] N. W. Ashcroft and N. D. Mermin, *Solid State Physics*, 1st ed. (Brooks Cole, Pacific Grove, CA, 1976).
- [2] C. Kittel, *Introduction to Solid State Physics*, 7th ed. (Wiley, Hoboken, NJ, 1995).
- [3] M. Tinkham and Physics, *Introduction to Superconductivity: Second Edition*, Second Edition edition (Dover Publications, Mineola, NY, 2004).
- [4] P. Phillips, *Advanced Solid State Physics*, 2 edition (Cambridge University Press, Cambridge, England, 2012).
- [5] G. Rickayzen, *Green's Functions and Condensed Matter*, Reprint edition (Dover Publications, Mineola, NY, 2013).
- [6] A. B. Mei, O. Hellman, N. Wireklint, C. M. Schlepütz, D. G. Sangiovanni, B. Alling, A. Rockett, L. Hultman, I. Petrov, and J. E. Greene, *Phys. Rev. B* **91**, 054101 (2015).
- [7] A. B. Mei, A. Rockett, L. Hultman, I. Petrov, and J. E. Greene, *Journal of Applied Physics* **114**, 193708 (2013).
- [8] C. V. Raman and N. S. N. Nathe, *Proc. Indian Acad. Sci. (Math. Sci.)* **2**, 406 (1935).
- [9] W. L. McMillan and J. M. Rowell, *Phys. Rev. Lett.* **14**, 108 (1965).
- [10] M. Holt, Z. Wu, H. Hong, P. Zschack, P. Jemian, J. Tischler, H. Chen, and T.-C. Chiang, *Phys. Rev. Lett.* **83**, 3317 (1999).
- [11] J. Wong, M. Wall, A. J. Schwartz, R. Xu, M. Holt, H. Hong, P. Zschack, and T.-C. Chiang, *Applied Physics Letters* **84**, 3747 (2004).
- [12] M. Holt, P. Zschack, H. Hong, M. Y. Chou, and T.-C. Chiang, *Phys. Rev. Lett.* **86**, 3799 (2001).
- [13] R. Xu, H. Hong, P. Zschack, and T.-C. Chiang, *Phys. Rev. Lett.* **101**, 085504 (2008).
- [14] B. M. Howe, E. Sammann, J. G. Wen, T. Spila, J. E. Greene, L. Hultman, and I. Petrov, *Acta Materialia* **59**, 421 (2011).
- [15] H.-S. Seo, T.-Y. Lee, I. Petrov, J. E. Greene, and D. Gall, *Journal of Applied Physics* **97**, 083521 (2005).
- [16] B. Howe, J. Bareno, M. Sardela, J. G. Wen, J. E. Greene, L. Hultman, A. A. Voevodin, and I. Petrov, *Surface & Coatings Technology* **202**, 809 (2007).
- [17] D. H. Mei, Y.-W. Kim, D. Lubben, I. M. Robertson, and J. E. Greene, *Applied Physics Letters* **55**, 2649 (1989).
- [18] P. Desjardins, T. Spila, O. Gürdal, N. Taylor, and J. E. Greene, *Phys. Rev. B* **60**, 15993 (1999).
- [19] R. C. Powell, N.-E Lee, Y.-W Kim, and J. E. Greene, *Journal of Applied Physics* **73**, 189 (1993).
- [20] F. Adibi, I. Petrov, L. Hultman, U. Wahlström, T. Shimizu, D. McIntyre, J. E. Greene, and J.-E Sundgren, *Journal of Applied Physics* **69**, 6437 (1991).
- [21] I. Petrov, P. B. Barna, L. Hultman, and J. E. Greene, *Journal of Vacuum Science and Technology A* **21**, S117 (2003).
- [22] X. Y. Zhang, J. S. Chawla, R. P. Deng, and D. Gall, *Phys. Rev. B* **84**, 073101 (2011).
- [23] D. Gall, C.-S. Shin, T. Spila, M. Odén, M. J. H. Senna, J. E. Greene, and I. Petrov, *Journal of Applied Physics* **91**, 3589 (2002).
- [24] H. Luo, G. Zou, H. Wang, J. H. Lee, Y. Lin, H. Peng, Q. Lin, S. Deng, E. Bauer, T. M. McCleskey, A. K. Burrell, and Q. Jia, *J. Phys. Chem. C* **115**, 17880 (2011).

- [25] Y. Zhang, N. Haberkorn, F. Ronning, H. Wang, N. A. Mara, M. Zhuo, L. Chen, J. H. Lee, K. J. Blackmore, E. Bauer, A. K. Burrell, T. M. McCleskey, M. E. Hawley, R. K. Schulze, L. Civale, T. Tajima, and Q. Jia, *J. Am. Chem. Soc.* **133**, 20735 (2011).
- [26] I. Petrov, F. Adibi, J. E. Greene, W. D. Sproul, and W.-D. Munz, *Journal of Vacuum Science and Technology A: Vacuum, Surfaces, and Films* **10**, 3283 (1992).
- [27] J. E. Greene, *Journal of Vacuum Science & Technology B* **1**, 229 (1983).
- [28] G. Gopalakrishnan, M. V. Holt, K. M. McElhinny, J. W. Spalenka, D. A. Czaplewski, T. U. Schüllli, and P. G. Evans, *Phys. Rev. Lett.* **110**, 205503 (2013).
- [29] J. Serrano, A. Bosak, M. Krisch, F. J. Manjón, A. H. Romero, N. Garro, X. Wang, A. Yoshikawa, and M. Kuball, *Phys. Rev. Lett.* **106**, 205501 (2011).
- [30] A. R. Oganov, M. J. Gillan, and G. D. Price, *The Journal of Chemical Physics* **118**, 10174 (2003).
- [31] W. Cochran and R. A. Cowley, *Journal of Physics and Chemistry of Solids* **23**, 447 (1962).
- [32] R. H. Lyddane, R. G. Sachs, and E. Teller, *Phys. Rev.* **59**, 673 (1941).
- [33] Y. Wang, J. J. Wang, W. Y. Wang, Z. G. Mei, S. L. Shang, L. Q. Chen, and Z. K. Liu, *J. Phys.: Condens. Matter* **22**, 202201 (2010).
- [34] M. Holt and T.-C. Chiang, *Phys. Rev. Lett.* **84**, 3734 (2000).
- [35] B. E. Warren, *X-Ray Diffraction* (Dover Publications, Mineola, NY, 1990).
- [36] J. Als-Nielsen and D. McMorrow, *Elements of Modern X-Ray Physics*, 2 edition (Wiley, Hoboken, NJ, 2011).
- [37] A. Segmüller, *Journal of Applied Physics* **43**, 2907 (1972).
- [38] D. Wilson and D. W. Bainbridge, *MT* **2**, 2925 (1971).
- [39] D. Chateigner, P. Germi, and M. Pernet, *Journal of Applied Crystallography* **27**, 278 (1994).
- [40] Bragg reflections are more localized than the diffuse TDS features. While the reciprocal space regions probed here are far from reciprocal lattice points relative to the width of Bragg reflections, the same regions may be close to reciprocal lattice points in comparison to the width of the diffuse TDS intensity. In addition, we adopt the convention of referring to reciprocal space directions, Brillouin-zone centers, and Bragg reflections by the corresponding lowest-integer Miller indices, i.e. [2 2 0] instead of [24 24 0]
- [41] M. J. L. Sangster, G. Peckham, and D. H. Saunderson, *J. Phys. C: Solid State Phys.* **3**, 1026 (1970).
- [42] A. Bosak and M. Krisch, *Phys. Rev. B* **72**, 224305 (2005).
- [43] D. W. Cooke, F. Hellman, J. R. Groves, B. M. Clemens, S. Moyerman, and E. E. Fullerton, *Review of Scientific Instruments* **82**, 023908 (2011).
- [44] O. Madelung, U. Rössler, and M. Schulz, Editors, *II-VI and I-VII Compounds; Semimagnetic Compounds* (Springer, Berlin, Germany, 1999), pp. 1–5.
- [45] E. Gmelin, *Cryogenics* **7**, 225 (1967).
- [46] E. Gmelin, *Journal of Physics and Chemistry of Solids* **30**, 2789 (1969).
- [47] P. Ferraro, S. Grilli, and P. D. Natale, *Ferroelectric Crystals for Photonic Applications: Including Nanoscale Fabrication and Characterization Techniques* (Springer Science & Business Media, 2013).
- [48] P. van der Sluis, *Journal of Physics D: Applied Physics* **26**, A188 (1993).

## 7. Figures

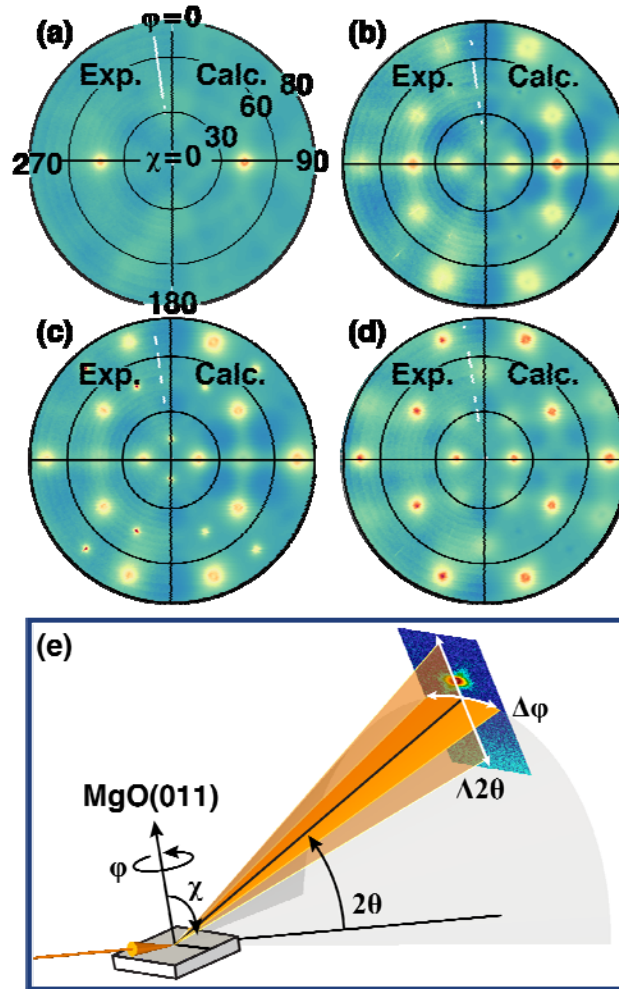


Figure 1. MgO(011) thermal-diffuse x-ray pole figures acquired with scattering vector  $q$  equal to (a) 57.82, (b) 62.61, (c) 64.42, (d) and 68.58  $\text{nm}^{-1}$ . The pole figures are plotted as normalized logarithmic isointensity maps over azimuthal angles  $\chi = 0-80^\circ$  and polar angles  $\phi = 0-360^\circ$ . The left side of each pole figure ( $180 < \phi < 360^\circ$ ) is determined using synchrotron radiation; the right side ( $0 < \phi < 180^\circ$ ) is computed from theoretical MgO phonon dispersion relations obtained by fitting experimentally-measured thermal-diffuse intensities, including those shown on the left side of each pole figure, to a model based on second-nearest-neighbor interatomic forces and long-range Coulombic interactions. (e) An illustration defining azimuthal  $\chi$ , rotational  $\phi$ , and Bragg  $2\theta$  angles with respect to the MgO crystal and an area detector.

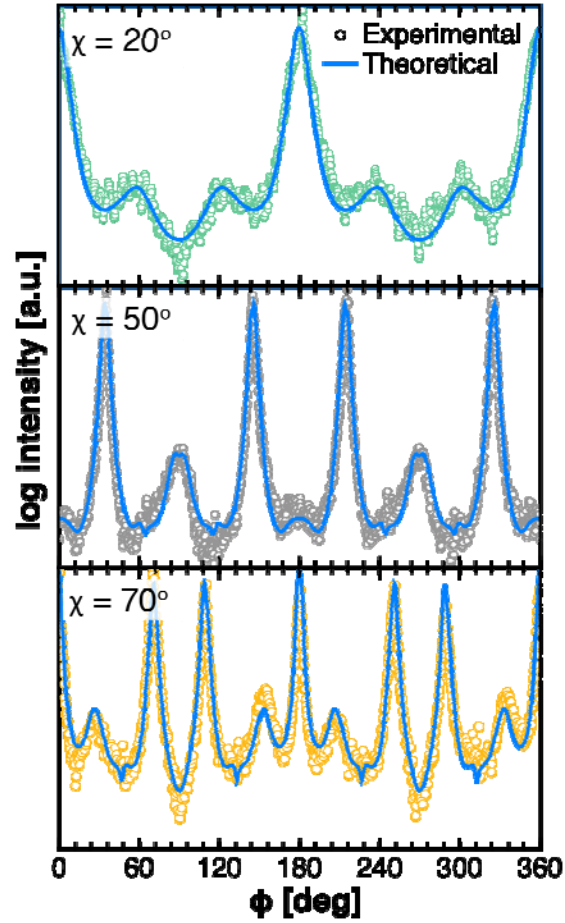


Figure 2. Typical MgO synchrotron thermal-diffuse x-ray intensity profiles (circles), plotted as a function of  $\phi$  between 0 and 360° with  $\chi = 20, 50$ , and 70°, obtained from the pole figure shown in Figure 1(d) acquired at scattering vector  $q = 68.58 \text{ nm}^{-1}$ . Simulated diffracted intensities (solid lines) calculated using MgO phonon dispersion relations obtained by fitting the measured pole-figure intensities using a model based on second-nearest-neighbor interatomic forces and long-range Columbic interaction parameters.



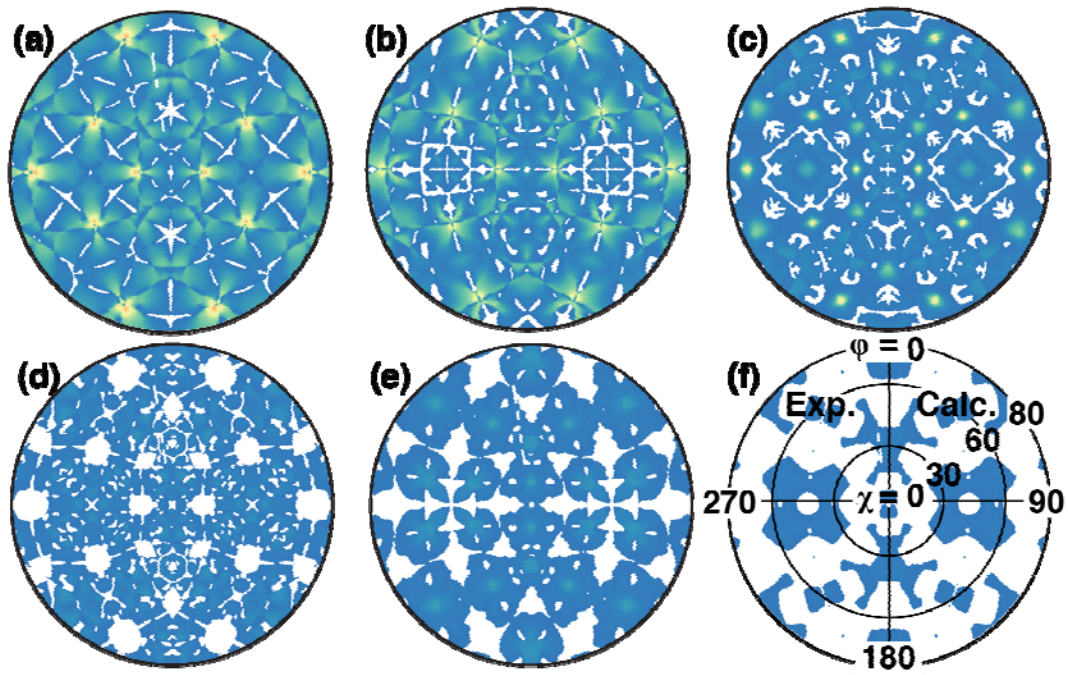


Figure 3. **Simulated** individual contributions from each phonon branch to MgO(011) thermal-diffuse pole-figure intensities acquired with scattering vector  $q = 68.58 \text{ nm}^{-1}$ . The panels (a), (b), (c), (d), (e), and (f) are in order of increasing phonon energy, with (a) corresponding to the lowest acoustic phonon branch, and (f) the highest optical branch. Plots are presented as logarithmic isointensity maps over azimuthal angles  $\chi = 0\text{--}80^\circ$  and rotational angles  $\phi = 0\text{--}360^\circ$ . The sum of intensities in (a)-(f) yields the diffracted thermal-diffuse intensity pole-figure plot shown Figure 1(d).

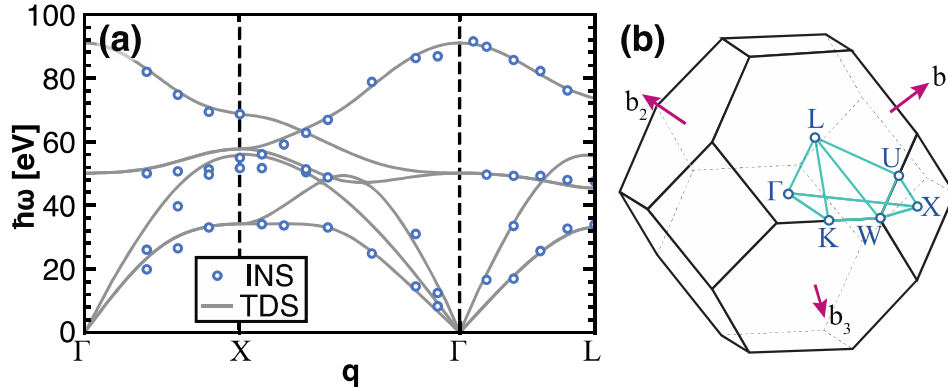


Figure 4. (a) MgO phonon dispersion relations (solid lines) obtained by fitting synchrotron reflection x-ray diffraction thermal-diffuse pole-figure intensities (Figures 1-2) using a model based upon second-order-interatomic forces and long-range Coulomb interactions. Points from inelastic neutron scattering (INS) experiments, Ref. [41], are shown for comparison. (b) The first Brillouin-zone of MgO showing high symmetry points corresponding to  $\Gamma$  [000], X [100], L [ $\frac{1}{2}\frac{1}{2}\frac{1}{2}$ ], W [ $\frac{1}{2}10$ ], U [ $\frac{1}{4}1\frac{1}{4}$ ], and K [ $\frac{3}{4}\frac{3}{4}0$ ]. Indices are in units of  $2\pi/a$  in which  $a$  is the MgO lattice parameter.  $b_1$ ,  $b_2$ , and  $b_3$  are reciprocal lattice vectors.

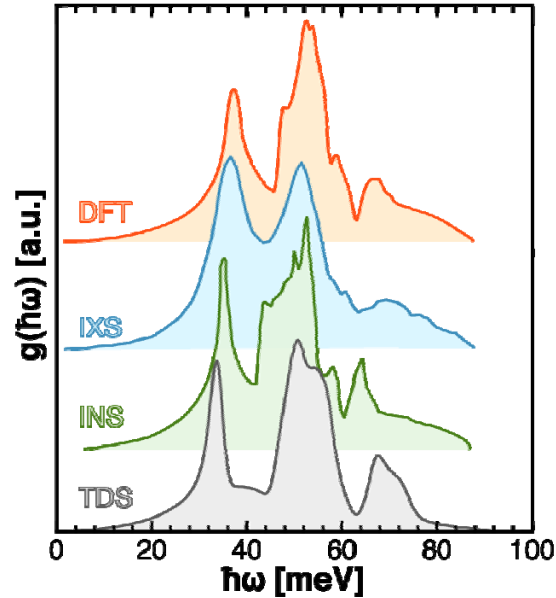


Figure 5. MgO phonon density of states  $g(\hbar\omega)$  (black line, lower TDS curve) obtained by fitting synchrotron x-ray diffraction thermal-diffuse pole-figure intensities (Figures 1-2) using a model based on second-order-interatomic forces and long-range Coulomb interactions. For comparison,  $g(\hbar\omega)$  curves from inelastic neutron-scattering experiments (green line, lower-middle INS curve) [41], inelastic x-ray scattering measurements (blue line, upper-middle INX curve) [42], and density-functional theory calculations (red line, upper DFT curve) [33] are also shown.

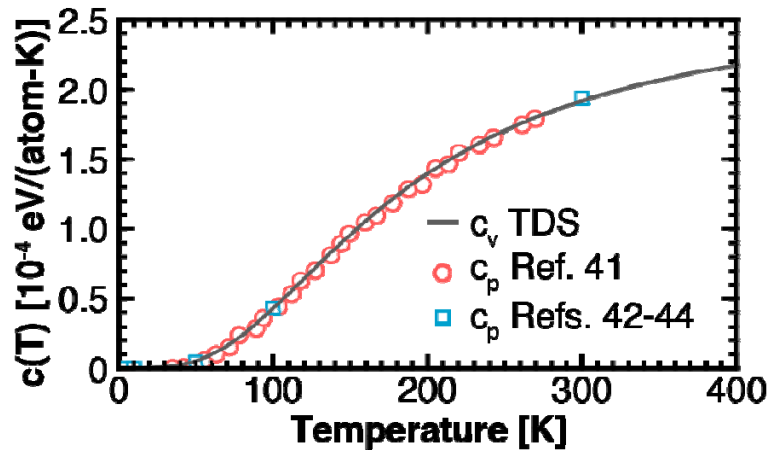


Figure 6. Temperature-dependent MgO isochoric heat capacities  $c_v(T)$  (solid line) calculated by fitting synchrotron x-ray diffraction thermal-diffuse pole-figure intensities (Figures 1-2), obtained at room-temperature, using a model based upon second-order interatomic forces and long-range Coulomb interactions. Squares and circles are isobaric heat capacities  $c_p(T)$  from Refs. [43] and [44–46], respectively.